NOVEMBER 10 2023

Principles of progressive slow-sound and critical coupling condition in broadband sonic black hole absorber

Xiang Yu ; Yongzhen Mi ; Wei Zhai ; Li Cheng

J. Acoust. Soc. Am. 154, 2988–3003 (2023)
https://doi.org/10.1121/10.0021880

JASA ARTICLE

Principles of progressive slow-sound and critical coupling condition in broadband sonic black hole absorber

Xiang Yu,[1] Yongzhen Mi,[2] Wei Zhai,[3] and Li Cheng[1,a)]
[1]Department of Mechanical Engineering, The Hong Kong Polytechnic University, Hong Kong 999077, Hong Kong
[2]Institute of High Performance Computing, A*STAR, Singapore 138632, Singapore
[3]Department of Mechanical Engineering, National University of Singapore, Singapore 117411, Singapore

ABSTRACT:
Recent advances in sonic black hole (SBH) provide new opportunities for controlling sound waves and designing wave manipulation devices. SBH is a device that consists of partitions with gradually decreasing inner radii inserted into an acoustic duct. Several studies have reported that SBH can achieve a broadband sound absorption coefficient close to 1, avoiding the issue of alternating high and low absorption coefficients observed in traditional sound absorbers. However, the fundamental mechanisms and principles behind this behavior are not yet fully understood. This study aims to investigate the detailed sound absorption mechanisms of SBH, including the progressive slow-sound effect and the critical coupling condition that leads to broadband sound absorption. To achieve this goal, an analytical model based on the effective medium approach is developed to investigate the layer-by-layer retardation in sound propagation. The sound absorption coefficient is then determined based on the surface impedance calculation. The effective medium analysis reveals that SBH enables a unique condition to progressively decelerate wave propagation across its layers. As a result, the critical coupling condition becomes more easily established with smoothly increasing SBH partitions and more discretised layers, as elucidated by the complex frequency analysis results. The physical insights gained from this study reveal the distinctive features of SBH compared to classical sound absorbers, paving the way for its engineering applications. © *2023 Acoustical Society of America*.
https://doi.org/10.1121/10.0021880
(Received 31 May 2023; revised 31 August 2023; accepted 29 September 2023; published online 10 November 2023)
[Editor: Siu-Kit Lau] Pages: 2988–3003

I. INTRODUCTION

The demand for broadband sound absorbers has been steadily increasing. Traditional sound absorbers that rely on viscous-thermal loss in porous structures and micro-orifices have been extensively researched.[1] However, these absorbers are limited by their sound absorption mechanisms, resulting in low absorption coefficients that are limited to either narrowband absorption bandwidths or ineffective bands. For example, foams and fabrics dissipate sound energy into heat, which is dependent on the flow resistance in the porous structure and the physical size of the absorber.[2,3] Non-fibrous sound absorbers, such as micro-perforated panels[4,5] and lattice structures,[6,7] have also been proposed, but their resonant nature typically leads to resonant sound absorption curves characterized by alternating high and low coefficients.

Recently, the development of acoustic metamaterials has emerged as a promising area of research for designing sound absorbers with subwavelength and broadband performances. The use of local resonances in layered structures has been proposed as a means to enhance sound absorption. Metamaterial systems, such as the periodic Helmholtz resonator (HR),[8] quarter-wave resonator (QWR),[9] metaporous sound absorber (MPSA),[10–12] and decorated membrane resonator,[13] have been actively studied for their potential applications as sound absorbers. These metamaterial systems have been found to induce unique physical properties, such as negative effective density and negative bulk modulus, which can inhibit sound wave transmission or enhance sound absorption in specific frequency ranges known as bandgaps. Recent studies have proposed the concept of complex frequency plane and critical coupling analysis to gain insights into the core mechanisms in metamaterials that lead to broadband or low-frequency sound absorption.[14] Resonators with graded dimensions can be coupled together to extend the working frequency of the absorber.[15] Such a design principle has been applied to create broadband absorbers composed of HR, QWR, and lattice elements.[7,16] However, this iterative process requires repeated fine-tuning of each layer until the resonance peaks are evenly spread out in split frequency bands,[15,17] and such manual tuning does not guarantee that all resonances remain critically coupled due to destructive interferences or manufacturing errors. As a result, a new approach to designing broadband sound absorbers is needed.

The novel concept of the sonic black hole (SBH) represents a promising breakthrough in the development of sound absorbers. The acoustic black hole (ABH), was originally

a)Email: li.cheng@polyu.edu.hk

https://doi.org/10.1121/10.0021880

proposed by Mironov,[18] who posited that a beam structure or acoustic duct with a gradually decreasing cross-sectional area could lead to continuous deceleration of wave speed, resulting in strong energy concentration and possible dissipation with external damping. In the context of sound absorption in air, this concept is referred to as the SBH.[19] While the structural ABH has been extensively studied over the past decade,[20,21] the acoustic SBH has received less attention. Only a few preliminary studies have investigated its sound absorption properties numerically and experimentally,[18,19,22] and its advantages have been showcased by reducing both sound reflection and transmission in an open-end SBH.[23,24] Additionally, combining SBH with a micro-perforated panel sound absorber results in enhanced sound absorption with an almost flat absorption curve close to 1,[25,26] a feature absent in existing resonant-type sound absorbers. Recent work experimentally proved that SBH can indeed slow down sound waves in the time domain.[27]

Despite the active investigations of SBH, the mechanisms underlying its sound dissipation have not been fully understood. The physical principles of SBH rely on the phenomenon of slow-sound, but it should be noted that slow-sound is not a unique characteristic of SBH. Many acoustic metamaterials present slow-sound effects owing to the dispersive properties of the embedded resonators, as studied in Refs. 11 and 28. For SBH, however, three questions remain unresolved: First, even if the wave velocity vanishes when the duct radius decays to zero, how the slow-sound effect behaves or varies specifically in each individual layer remains unknown. Second, the relationship between the slow-sound effect and the complementary damping required to promote the critical coupling condition is unclear. Third, how these two physical effects—slow-sound and damping—vary or compete with each other with different SBH parameters has never been investigated.

This paper aims to answer the above three questions and elucidate the sound dissipation mechanism of SBH. Following this introduction, Sec. II elaborates a layer-by-layer scheme to investigate the sound propagation speed and effective medium properties in a SBH. The sound absorption coefficient is then determined based on the resultant surface impedance. The distinctive features of SBH are compared with traditional sound absorbers, such as quarter-wave resonator array (QWRA) and MPSA. Complex frequency plane analysis is then performed to reveal the effect of damping in fulfilling the critical coupling condition. The analysis shows that SBH is superior to traditional sound absorbers, as it requires much less damping to absorb broadband sound, due to its rainbow-like sound trapping mechanism. Section III further examines the geometric parameters associated with SBH design, including the layer numbers, total length, and order of the decaying profile. It is shown that SBH with more discretised layers enables smoother variation of sound speed and more uniform distribution of coupled resonances in the frequency domain. The identified modes in the complex frequency plane are closer to the real frequency axis to achieve critical coupling, thus, demanding less damping treatment to maximize sound absorption. The length of SBH and the order of the profile are also investigated to show their effects on the cut-on frequency and the critical coupling condition.

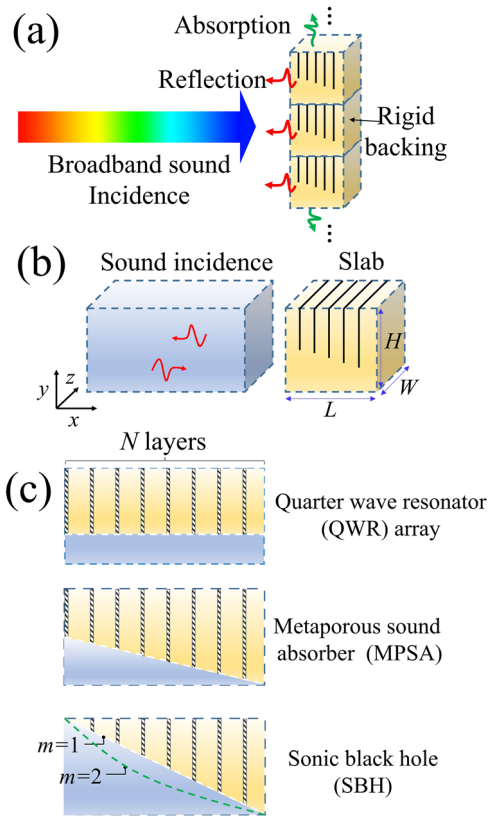

FIG. 1. (Color online) (a) An illustration of the acoustic system composed of periodic unit cells to absorb broadband noise. (b) A unit cell slab with dimensions $L \times H \times W$ under normal sound incidence. (c) Schematics of three unit cell designs corresponding to QWRA, MPSA, and SBH.

II. FORMULATION OF THE PROBLEM

A. Geometric parameters

Figure 1(a) depicts a potential design for a sound-absorbing surface capable of absorbing broadband sound waves based on metamaterial unit cells. The surface is composed of periodic unit cells with rigid backing, and the entire domain is filled with air of sound speed c_0 and density ρ_0. At the interface, incident sound energy is reflected back or absorbed, depending on the impedance condition of the metamaterial surface. For sound waves of normal incidence, the sound absorption characteristics of the periodic surface can be analyzed using a representative unit cell, as shown in Fig. 1(b). The dimensions of the unit cell slab in the x, y, z directions are L, H, W, respectively. The slab width W is assumed to be infinite in the z direction, so that the problem under investigation reduces to a two-dimensional (2D) system in the xy plane.

Our interest is to design a slow-sound absorber to achieve broadband sound absorption. Traditionally, to enhance sound absorption in selected frequencies, resonators are often designed with partitions or cavities added to a porous material. Figure 1(c) depicts the schematics of

common resonator-embedded sound absorbers, including QWRA and MPSA. QWRA consists of periodic HRs or quarter-wave tubes with identical geometry. They can perfectly absorb sound near the resonance frequency, but the effective bandwidth is typically narrow, and very low absorption coefficients occur at non-resonating frequencies. To broaden the frequency range, MPSA overlaps the resonances of multiple resonators at different frequency regions, which is practically achieved by incorporating partitions with varying heights. The partition heights can either monotonically increase or decrease, or they can be randomly distributed.[11] However, MPSA requires fine-tuning of the constituting layers to separate the resonances. Upon completing the geometric tuning, MPSA still requires significant damping to ensure effective sound absorption is maintained over the desired frequencies.

In contrast to the previous two cases, the design of the SBH features unique geometric characteristics. Although its cross section still resembles a series connection of quarter-wave resonators formed by rigid partitions, the SBH geometry possesses two distinguishing features. First, the height of the partition at the entrance is null, creating a smooth transition and impedance matching from the incident domain to the SBH slab. Second, the partitions adopt a smoothly varying profile with a geometric order of m that reaches the end. The geometry of the SBH is defined by its height H, length L, geometric order m, number of layers N, and the thickness of individual partitions.

We seek to understand the sound propagation characteristics and the variation of sound speed across the constituting layers. The unit cell is first discretised into N layers by the rigid partitions, as shown in Fig. 2(a). To demonstrate the major differences in the sound absorption mechanisms and performances, the SBH is compared with two conventional forms of absorbers, namely, the QWRA and MPSA. To ensure a fair comparison, the dimensions of the slab are set to be identical with $L = 0.03$ m and $H = 0.03$ m. The internal geometries of each layer can be specified by the height of the partition b_N and the void height h_N. Note that $b_N + h_N = H = 0.03$ m. For the three compared cases, b_N and h_N are defined as follows:

(1) QWRA: The height of the partitions and the gaps they leave at each layer are identical, i.e., $b_1 = b_i = b_N$, $h_1 = h_i = h_N$.
(2) MPSA: The MPSA investigated in Ref. 11 is taken as a reference for comparison. It has partition heights that monotonically increase from $b_1 = 0.018$ m to $b_N = 0.028$ m, where the number of layers is $N = 6$. The heights of the voided gaps, therefore, vary from $h_1 = 0.012$ m to $h_N = 0.002$ m.
(3) SBH: The height of the partitions follows a monotonically increasing profile from 0 to H. The number of partitions and the discretised layers are both N. The height of the partitions and the voided gaps can be expressed as

$$b_i = [(i-1)\Delta L/L]^m H,$$
$$h_i = H - [(i-1)\Delta L/L]^m H,$$

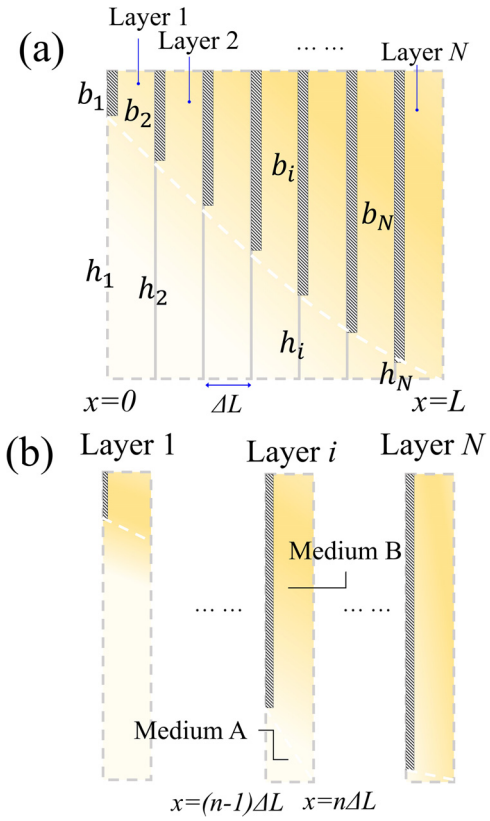

FIG. 2. (Color online) The unit cell is discretised into N layers according to the partitions. The effective medium properties of each layer, including effective density, bulk modulus, and the effective sound speed in the positive x direction, can be derived explicitly.

where m is the order of the SBH. For integer m, $m = 1$ refers to linear SBH, $m = 2$ refers to quadratic SBH, and $m = 3$ refers to cubic SBH. ΔL is the discretised length of the ith layer. To reduce the number of possible cases, the partitions are assumed to be equally spaced, so that $\Delta L = L/N$. The thicknesses of the partitions are all assumed as t to reduce the number of variables.

B. Effective medium properties

Figure 2 depicts the unit cell, which is divided into N layers based on the partitions, and the effective medium properties of each layer, including the effective density, bulk modulus, and effective sound propagation speed in the positive x direction, can be derived explicitly. As shown in Fig. 2(b), at each local layer i, the volume corresponding to the narrowing duct is denoted as medium A, while that bounded by the partitions is denoted as medium B. Physically speaking, the dispersive property of medium A_i is affected by medium B_i due to the mismatch of cross-sectional area and the embedded resonance in medium B_i. At the interface between the two media, the impedance of the tube section of B_i can be expressed as

$$Z_{i,B} = -\frac{j\rho_B c_B}{\phi_i}\cot[k_B(H - h_i)], \quad (1)$$

https://doi.org/10.1121/10.0021880

where k_B is the wavenumber in medium B. ϕ_i is the volumetric ratio of the air in medium B, which is defined by the thicknesses of the partition and the discretised layer, $\phi_i = 1 - t/\Delta L$. The interface between medium A and B is inclined, so the height of the ith layer h_i is taken as the average of the heights on the left and right sides. Note that ΔL, the discretised layer length, is assumed to be smaller than half of the acoustic wavelength, so that sound propagation in medium B can be simplified as one-dimensional, i.e., only vertical mode. For $\Delta L < 1$ cm, such an assumption is valid up to around 17 000 Hz.

The wavenumber in medium A can be decomposed into propagation components in the x and y directions, as

$$k_{i,A}^2 = k_{i,A,x}^2 + k_{i,A,y}^2. \tag{2}$$

The sound pressure field of medium A can be written as

$$P_{i,A}(x,y) = a_i e^{jk_{i,A,x}x}\cos(k_{i,A,y}y), \tag{3}$$

such that the velocity in the y direction can be derived as

$$\frac{\partial P_{i,A}(x,y)}{\partial n_y} = -j\rho\omega V_{i,A,y}. \tag{4}$$

Combining Eqs. (3) and (4), the velocity $V_{i,A,y}$ can be obtained as

$$V_{i,A,y} = \frac{a_i k_{i,A,y}\sin(k_{i,A,y}y)}{j\rho\omega} e^{jk_{i,A,x}x}. \tag{5}$$

At the interface between medium A and B where $y = h_i$, $P_{i,A}(x,y)/V_{i,A,y} = Z_{i,B}$ leads to

$$\frac{j\rho_A\omega\cot(k_{i,A,y}h_i)}{k_{i,A,y}} = -\frac{j\rho_B c_B}{\phi_i}\cot[k_B(H-h_i)]. \tag{6}$$

Assuming that media A and B have a common air density $\rho_A = \rho_B$, Eq. (6) can be rearranged into

$$-\phi_i k_B \tan[k_B(H-h_i)] = k_{i,A,y}\tan(k_{i,A,y}h_i). \tag{7}$$

The above transcendental equation can only be solved numerically, or its solution can be approximately solved by making a small angle assumption, i.e., $\tan(k_{i,A,y}h_i) \approx k_{i,A,y}h_i$, such that

$$\begin{aligned} k_{i,A,y}^2 &= -\phi_i k_B \tan[k_B(H-h_i)]/h_i, \\ k_{i,A,x}^2 &= k_{i,A}^2 - k_{i,A,y}^2 = k_A + \phi_i k_B \tan[k_B(H-h_i)]/h_i. \end{aligned} \tag{8}$$

Such approximation gives accurate results of $k_{i,A,x}$, $k_{i,A,y}$ in the low frequencies. The possible error caused by the approximation is discussed in the Appendix.

Assume $k_A = k_B = k$, $k_{i,A,x}$ is reduced to $k_{i,A,x} = k\sqrt{[1+\phi\tan[k(H-h_i)]/kh_i}$. Finally, the sound propagating velocity in the ith effective layer in the x direction can be derived as

$$c_{i,A,x}^e = c_0/\sqrt{1+\phi_i\tan[k(H-h_i)]/kh_i}. \tag{9}$$

It can be seen that the effective sound speed of the ith layer is directly related to h_i. Generally, decreasing h_i toward the end of the SBH decelerates the sound speed $c_{i,A,x}^e$ in each layer. If the voided height h_i is compressed to a very small value by a long partition, then $c_{i,A,x}^e \to 0$ means that sound speed is decelerated to zero at the end.

The effective medium properties of the ith layer, namely, the effective density $\rho_{i,A}^e$ and the bulk modulus $\kappa_{i,A}^e$, can be further obtained as

$$\begin{aligned} \rho_{i,A}^e &= \rho_0/(1-b_i/H), \\ \kappa_{i,A}^e &= \kappa/(1-b_i/H)\sqrt{1+\phi_i\tan[k(H-h_i)]/kh_i}. \end{aligned} \tag{10}$$

C. Surface impedance and absorption coefficient

The sound absorption coefficient is further obtained by deriving the acoustic impedances of the discretised layers and the final surface impedance of layer 1 connecting to the incident domain. The surface impedance of the ith layer Z_i^e can be expressed as[29]

$$Z_i^e = z_i^e\frac{Z_{i+1}^e + jz_i^e\tan(k_i^e L_i)}{jZ_{i+1}^e\tan(k_i^e L_i) + z_i^e}, \quad i = 1,2,\ldots,N. \tag{11}$$

where $z_i^e = \sqrt{\rho_{i,A}^e\kappa_{i,A}^e}$ is the effective impedance of the ith layer determined according to the effective density $\rho_{i,A}^e$ and the effective bulk modulus $\kappa_{i,A}^e$ in Eq. (10). The above equation is solved successively backward from layer $i = N$, where its impedance is expressed as

$$Z_N^e = -jz_N^e\cot(k_N^e L_N). \tag{12}$$

By repeating the calculations, the surface impedance of the first layer Z_1^e is solved. The acoustic impedance consists of two parts, the air resistance based on the real part [Re(Z)] and the air mass reactance, based on the imaginary [Im(Z)]. Physically speaking, the resistance describes the friction and energy loss in the structure, whilst the reactance determines the frequency where highest dissipation occurs. The reflection coefficient for sound pressure is then given by

$$R = (Z_1^e - z_0)/(Z_1^e + z_0), \tag{13}$$

where $z_0 = \rho_0 c_0$ is the impedance of air. Finally, the absorption coefficient is calculated as $\alpha = 1 - |R|^2$. To achieve total sound absorption, i.e., $\alpha = 1$, it is noted from Eq. (12) that Re(Z) and Im(Z) should be ideally 1 and 0, respectively. Numerical calculations of the acoustic impedance and absorption coefficient curve were coded using MATLAB. To understand the generic effect of damping in the proposed systems, complex sound speed is assumed as $c^* = c_0(1+\eta j)$, where the imaginary part η denotes an isotropic loss factor. If certain types of porous material or narrow tubes need to be

accurately modelled, it is very straightforward to characterize them as an equivalent fluid domain by a complex valued mass density and bulk modulus.[22,30,31]

D. Complex frequency plane analysis

The performance of the sound-absorbing unit cell is closely related to the presence of loss in the system. To investigate this aspect, a complex frequency plane analysis[14] is performed by calculating the reflection coefficient in the logarithmic scale while varying the imaginary part of the wavenumber. In the absence of loss, the reflection coefficient exhibits pairs of zeros and poles that are complex conjugate and symmetric with respect to the real frequency axis. The imaginary part quantifies the radiation leakage and also indicates the amount of damping required to achieve complete absorption. When loss is introduced, the zeros will approach the real frequency axis, and critically coupling conditions are established when losses perfectly balance the radiation leakage. The use of complex frequency representation enables us to reveal the unique feature of SBH, which exhibits a continuous and evenly distributed set of resonances, making it possible to achieve broadband sound absorption with lower damping requirements.

III. MECHANISM OF SOUND ABSORPTION: SLOW-SOUND AND CRITICAL COUPLING

This section aims to investigate and compare the sound absorption performance of the three different unit cells illustrated in Fig. 1(c) and analyze their underlying mechanisms. The outer dimensions of the unit cells are fixed as $L = 0.03$ m, $H = 0.03$ m, and the thickness of the partitions is set to be 0.0002 m. To simplify the analysis and enhance computational efficiency, a 2D model is assumed with infinite width W. The sound absorption coefficient is calculated by utilizing the surface impedance expressions given in Eqs. (11)–(13). Optimal sound absorption is achieved when the real and imaginary parts of the impedance reach ideal values, i.e., resistance $\mathrm{Re}(Z) \approx 1$ and reactance $\mathrm{Im}(Z) \approx 0$. The propagation speed of sound in the duct is described by Eq. (9). A complex frequency plane analysis is performed to illustrate the impact of damping on the sound absorption performance.

A. Slow-sound effect

We begin with the baseline case consisting of an array of QWRs as shown in Fig. 1(c). The partition height is set identically as 0.02 m; therefore, $b_i = 0.02$ m and the voided gap $h_i = 0.01$ m. The number of discretised layers is $N = 10$, and the damping loss factor is taken as $\eta = 0.05$. Figure 3 depicts the physical properties and absorption performance of the QWRA unit cell. In Fig. 3(a), the sound speed of all layers in the QWRA overlaps to a single curve, which is approximately 0.55 of the original sound speed in air, $0.55c_0$, for frequencies below 3000 Hz. This is because all the layers possess the same partition height b_i and h_i, as can be inferred from Eq. (9). The sound speed is further compressed down starting from 4000 Hz. For the effective density, identical b_i values result in a constant curve, as seen in Fig. 3(b). The effective bulk modulus of the constituting layers in Fig. 3(c) turns to negative values at 4200 Hz, agreeing with the resonant frequency of the QWR calculated as $c_0/4/b_i = c_0/4/0.02 = 4250$ Hz. In Fig. 3(d), the sound absorption coefficient of the QWR array calculated using the impedance matching technique shows a distinct peak near 4000 Hz, where α approaches 1 for perfect absorption. The characteristic impedance of the QWR normalized by air

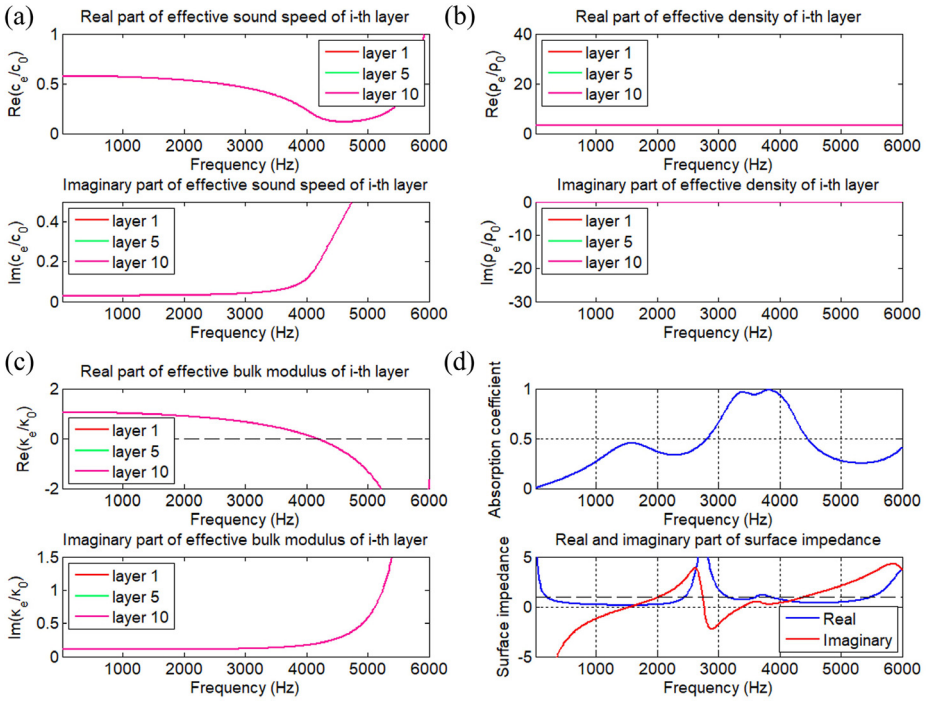

FIG. 3. (Color online) QWRA, $N = 10$, $h_i = 0.01$ m, $\eta = 0.05$: the sound speed and effective properties of the ith layer and the absorption coefficient. (a) Real and imaginary parts of effective sound speed of the ith layer; (b) real and imaginary parts of effective density of the ith layer; (c) real and imaginary part of bulk modulus of the ith layer; (d) absorption coefficient of the unit cell obtained using impedance matching calculation and the real and imaginary parts of the surface impedance.

https://doi.org/10.1121/10.0021880

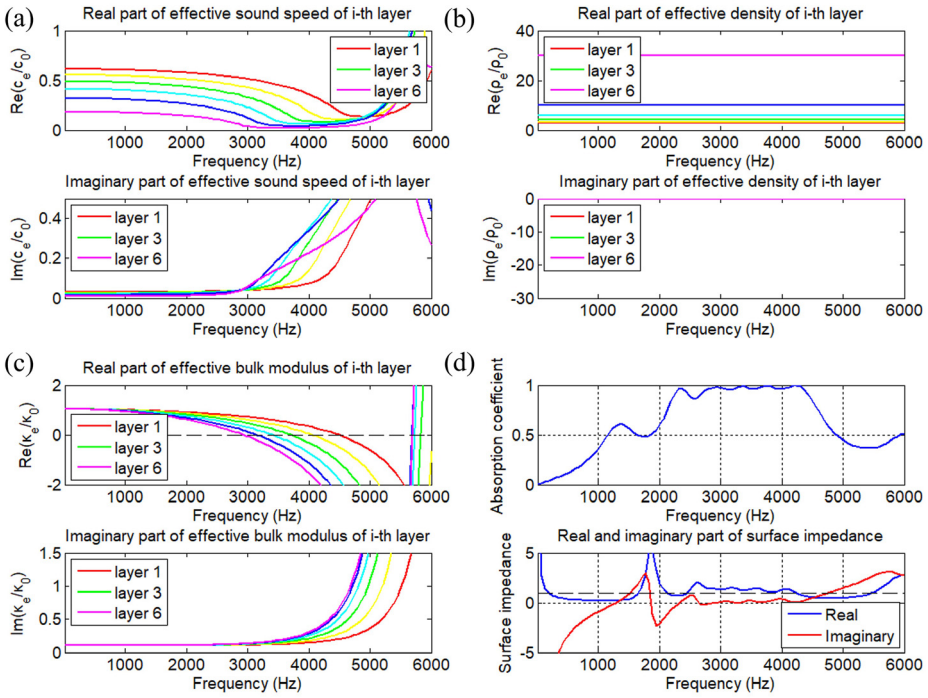

FIG. 4. (Color online) MPSA, $N=6$, $h_1=0.012$ m, $\eta=0.05$: the sound speed and effective properties of the ith layer and the absorption coefficient. (a) Real and imaginary parts of effective sound speed of the ith layer; (b) real and imaginary parts of effective density of the ith layer; (c) real and imaginary part of bulk modulus of the ith layer; (d) absorption coefficient of the unit cell obtained using impedance matching calculation and the real and imaginary parts of the surface impedance.

impedance Z_0 shows that the resistance (real part of impedance Z) is close to 1 in this frequency region, where the reactance (imaginary part of impedance Z) vanishes. This fulfills the condition to achieve $\alpha=1$, as indicated by Eq. (13). At other frequencies, perfect impedance matching conditions were not observed, resulting in mostly low α values. These observations align with the traditional theory of sound absorption by QWR.

Second, the physical properties and absorption performance of MPSA[10–12] are analyzed in detail. The geometric parameters of the MPSA are taken from Ref. 11, where six layers ($N=6$) with inner height linearly increasing from $b_1=0.012$ m to $b_6=0.03$ m are defined. The partition height at the ith layer is, therefore, $b_i=0.012+0.002i$ m. The same damping loss factor $\eta=0.05$ is assumed. Figure 4(a) shows that the sound speeds of the constituting layers are decreased on a layer-by-layer basis. In low frequencies below 2000 Hz, the decrement from layer 1 to layer 6 is roughly from $0.6c_0$ to $0.2c_0$. Between 2000 and 5000 Hz, the sound speeds of the last few layers are further compressed down to nearly zero. Above 5000 Hz, the sound speeds rapidly rise back to original c_0. The imaginary parts of sound speed, which is related to damping loss factor, generally rise above 3000 Hz, with the loss being generally higher in the layers with longer partitions in medium B and shorter voids in medium A. The effective density in Fig. 4(b) shows six constant curves due to the six partition heights b_1 to b_6. As indicated by Eq. (10), the effective density is simply a function of the partition height, not a function of the frequency. The effective bulk modulus in Fig. 4(c) shows negative regions crossing the zero axis at different frequencies for different layers. The last layer $i=6$ closest to the termination (partition height $b_6=0.028$ m) has a starting frequency as low as 3000 Hz, whereas the first layer $i=1$ at the entrance (partition height $b_1=0.018$ m) has a starting frequency of 4500 Hz. Overall, the curves corresponding to layers 1–6 show a distribution of slow-sound effect and negative effective properties between 3000 and 4500 Hz, but the distribution is not uniform and is capped at a frequency limit. The absorption coefficient in Fig. 4(d) shows that α achieves nearly 1 in this frequency range, and the characteristic impedance confirms the ideal impedance matching condition with resistance ≈ 1 and reactance ≈ 0.

For the third case, a linear SBH with geometric parameters selected as $N=20$, $m=1$, $\eta=0.05$ is analyzed. Figure 5 presents the slow-sound behavior and the effective properties for layers 1–20. Figure 5(a) shows that the sound speed in the discretised layers decreases more smoothly from c_0 to $0.2c_0$, forming a nice rainbow pattern that evenly fills the entire frequency domain. Despite the finite number of discretised layers, the overall slow-sound effect is progressive, continuous, and smooth. Below 3000 Hz, the imaginary parts of sound speeds remain low, with a drastic increase observed thereafter, indicating high potential for sound absorption. The effective density in Fig. 5(b) again shows flat curves. Figure 5(c) shows that frequency points where the effective bulk modulus crosses the zero axis to negative regions are more evenly distributed between 3000 and 6000 Hz. This contrasts with the previous cases where the usable frequency range is either singular or limited. The absorption coefficient in Fig. 5(d) shows that perfect sound absorption with $\alpha=1$ starts from 3000 Hz, and good performance is maintained at high frequencies. The characteristic impedance shows that ideal impedance matching condition occurs from 3000 Hz and holds up to the highest frequencies.

The sound absorption coefficients of the three compared cases, as analyzed above, are compared in Fig. 6(a). Note that the layer numbers in the QWR, MPSA, and SBH are

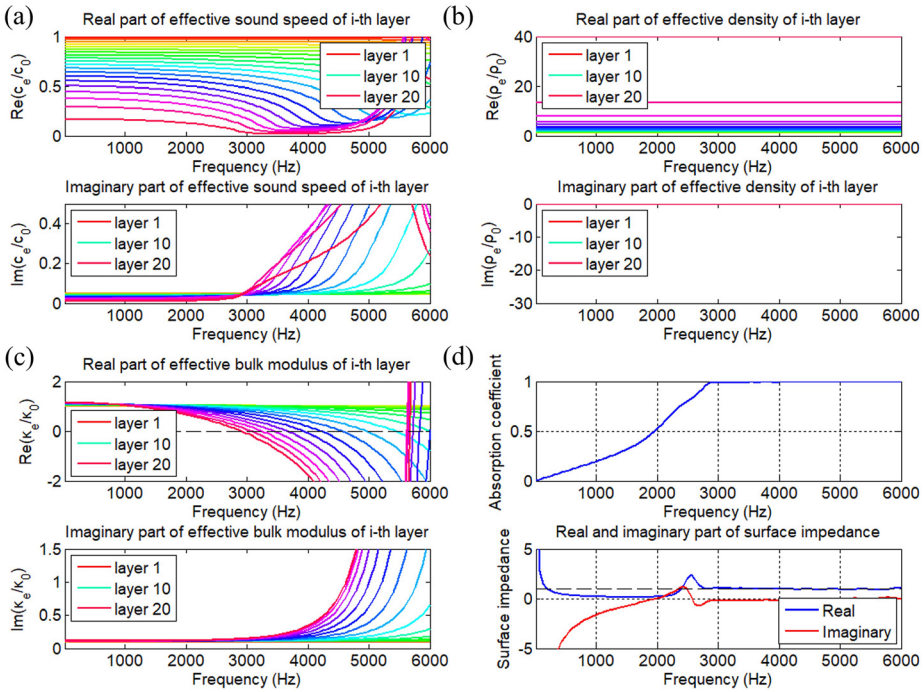

FIG. 5. (Color online) SBH, $N = 20$, linear $m = 1$, $\eta = 0.05$: the sound speed and effective properties of the ith layer and the absorption coefficient. (a) Real and imaginary parts of effective sound speed of the ith layer; (b) real and imaginary parts of effective density of the ith layer; (c) real and imaginary parts of bulk modulus of the ith layer; (d) absorption coefficient of the unit cell obtained using impedance matching calculation and the real and imaginary parts of the surface impedance.

$N = 10$, 6, and 20, respectively. Obviously, the SBH shows the highest and widest-band absorption performance, with an effective bandwidth nearly doubled and tripled compared with the MPSA and QWRA, respectively. From 2000 to 6000 Hz, the average sound absorption coefficient of SBH is 0.943, and it is 0.762 for the MPSA and 0.535 for the QWRA. In terms of the effective bandwidth, the proportion of the absorption coefficient above 0.6 between 1000 and 6000 Hz is 78.9% for the SBH, 48.4% for the MPSA, and 22.9% for the QWRA. The analyses on sound propagation speed and effective medium properties confirm that such drastic improvement is attributable to the progressive slow-sound effect and perfect impedance matching conditions with evenly distributed partition lengths. For a fairer comparison, Figs. 6(b)–6(d) further compare QWR, MPSA, and SBH with the same number of layers, where $N = 6$, 10, and 20, respectively. It can be seen that for all cases, SBH generally outperforms the other two absorber configurations in most of the frequencies. The absorption curve is higher and flatter and maintains at a high value close to 1 toward high frequencies, provided that the layer number is high enough ($N \geq 10$ in the case here). Therefore, the SBH is superior to both the MPSA and QWRA in terms of broadband sound absorption performance. Section III B will detail the study of the effect of layer numbers, damping loss factor, and other parameters affecting the performance of SBH.

B. Critical coupling condition

To gain further insight into the differences in sound absorption mechanisms and the superior performance of SBH, the complex frequency plane representation of the reflection coefficient in logarithmic scale is shown in Fig. 7, where $20\log_{10}(|R|)$ is plotted in a 2D plane by varying the frequency [thus, the value of Re(KL)] and linearly sampling the value of Im(KL).[32] The frequency range is selected to be from 1800 to 5400 Hz, corresponding to a normalized frequency range of Re(KL) from 1 to 3. The damping loss factor is first set as $\eta = 0$ to observe the lossless eigenmodes in the complex frequency plane. The illuminated spots denote zero-pole pairs. These modes, being energy-leaking, need to be compensated by adding damping for sound absorption. The quality factor of the resonances can be quantified by $Q = \mathrm{Re}(f)/[2\mathrm{Im}(f)]$. Higher quality factor, therefore, means smaller imaginary part and larger real part, which facilitates better sound absorption with less requirement for damping.

By observing the first row of Fig. 7, where damping η is kept at zero, the first case with QWRA shows three distinct pairs of zero-pole between 3000 and 4000 Hz, correlating with the peak locations in the sound absorption coefficient curve in Fig. 2(d). The second case with MPSA shows more zero-pole pairs, indicating that the system incorporates more resonance modes to cope with a wider frequency range. In contrast, the third SBH case has over ten pairs of uniformly distributed zeros and poles above 3000 Hz. While still discrete, the distribution is nearly continuous, with no two pairs overcrowding the same frequency range. It can also be seen that as frequency increases, the value of the imaginary part increases, thereby decreasing the quality factor.

Rows 2–4 of Fig. 7 illustrate the effect of damping losses on the system as the damping loss factor η increases from 0 to 0.01, 0.03, and 0.05. For all three resonant absorber cases, the zeros gradually move closer to the real frequency axis with increasing damping, indicating a better coupling condition, which is essential for achieving perfect absorption. Complete sound absorption occurs when the radiation leakage is perfectly compensated by the added losses, with zeros lying on the real frequency axis. Apart

https://doi.org/10.1121/10.0021880

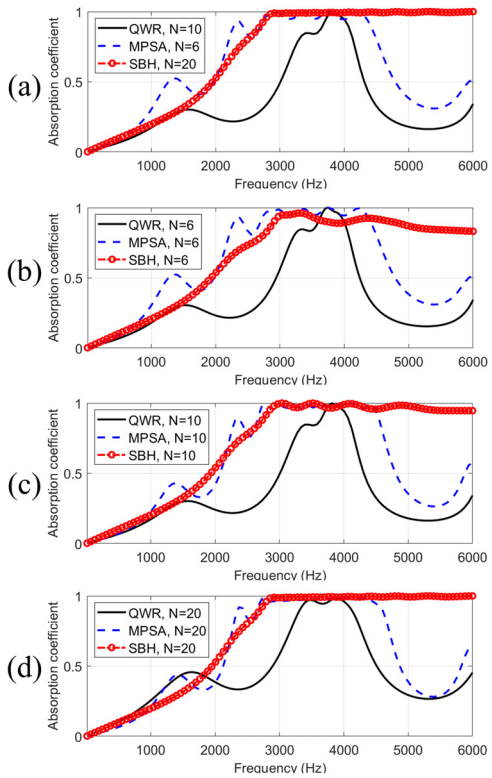

FIG. 6. (Color online) Comparison of sound absorption coefficients across three different unit cell configurations: (a) the configurations as analyzed in Figs. 3–5 are directly compared, where the layer numbers in the QWR, MPSA, and SBH are $N = 10$, 6, and 20, respectively. (b)–(d) QWR, MPSA, and SBH with the same number of layers are compared, where $N = 6$, 10, and 20, respectively.

from that, one can also observe that the zeros of the SBH case move faster than the other two cases when the damping loss factor increases from 0.01 to 0.03. Perfect absorption condition in wide frequency range has already been achieved with $\eta = 0.03$ for the SBH case. Further increasing damping from 0.03 to 0.05 moves zeros below the real frequency axis, which may not be necessary.

Based on the above understanding of the coupled modes and the effect of damping on the critical coupling condition, Fig. 8 presents the variation of absorption coefficients for each type of absorber with increasing levels of damping, $\eta = 0.01$, 0.03, and 0.05, respectively. Both QWR and MPSA exhibit low sound absorption with low damping, and they demonstrate a consistent trend of enhanced sound absorption as damping loss increases. In contrast, Fig. 8(c) shows that the SBH absorbs sound with far less dependence on high damping loss factors. The increment from $\eta = 0.03$ to 0.05 is less apparent as compared to $\eta = 0.01$–0.03, especially for frequencies above 3000 Hz, where the SBH effect has been established. This provides evidence of the energy focalization effect, which allows absorption to take place with less damping. In summary, based on the selected geometric configurations, the advantages of the SBH absorber have been demonstrated through detailed comparisons of the slow-sound effect, even distribution of effective medium properties, highly smooth absorption curve with $\alpha = 1$ maintaining at high frequency, and less dependence on high damping loss factor.

IV. EFFECT OF GEOMETRY AND DAMPING LOSS ON THE SBH ABSORPTION

In Sec. III, the underlying principles behind the exceptional sound absorption behaviors of the SBH were clearly analyzed. We now focus on the effects of geometry and damping loss. To do so, the geometric parameters of the SBH, including the total layer numbers N, total length L, and profile order m, are selected as variables. The SBH height ($H = 0.03$ m) and the partition thickness ($t = 0.0002$ m) remain unchanged.

A. Effect of layer numbers *N* with fixed total length

We first investigate the effect of varying the number of internal layers N in a SBH with a fixed total length to observe its effect on the sound speed and critical coupling condition. Using the linear SBH case with $m = 1$, three variations with $N = 6$, $N = 10$, and $N = 20$ are compared here. The total length L is fixed at $L = 0.03$ m, and the lossless case with $\eta = 0$ is first calculated. Figures 9(a)–9(c) show the real part and imaginary part of effective sound speed for the compared cases. It can be seen that more discretised layers allow more even distribution of the slow-sound effect, resulting in continuous sound speed reduction without abrupt changes at interfaces. The imaginary part curves are all zero because $\eta = 0$. Figures 9(d)–9(f) show that with a larger N, the zeros in the complex frequency plane are intrinsically closer to the real frequency axis, which implies that less damping is required to fully maximize sound trapping and dissipation when the SBH layers are sufficiently discretised.

To further investigate the effect of layer numbers in the presence of damping, Fig. 10 presents the sound absorption coefficient curves and the complex frequency planes for the same cases with varying damping loss factor $\eta = 0.01$, 0.03, and 0.05. The results show that as η increases from 0.01 to 0.05, the case with fewer layers exhibits a higher increment in sound absorption. In contrast, the curve with $N = 20$ remains nearly unchanged, with η increasing from 0.03 to 0.05, particularly for frequencies above 3000 Hz. This finding is somewhat counterintuitive, as higher damping usually leads to higher energy absorption, and the increment is thought to be an add-on effect that is not coupled to the geometric factors. A closer examination of the resonance modes in the complex frequency planes reveals that the zero-pole pairs are closer to the real frequency axis for the case with more discretised layers. Therefore, less damping is required to balance the radiation leakage, enabling perfect sound absorption with a low value of η. This finding is of vital significance in practical implementation, as increasing damping through specially designed porous materials is not always feasible or desirable. Less dependence on damping value also indicates that the SBH can absorb sound with the inherent loss between the narrow partitions, which is one of its striking features. Although not rigorously

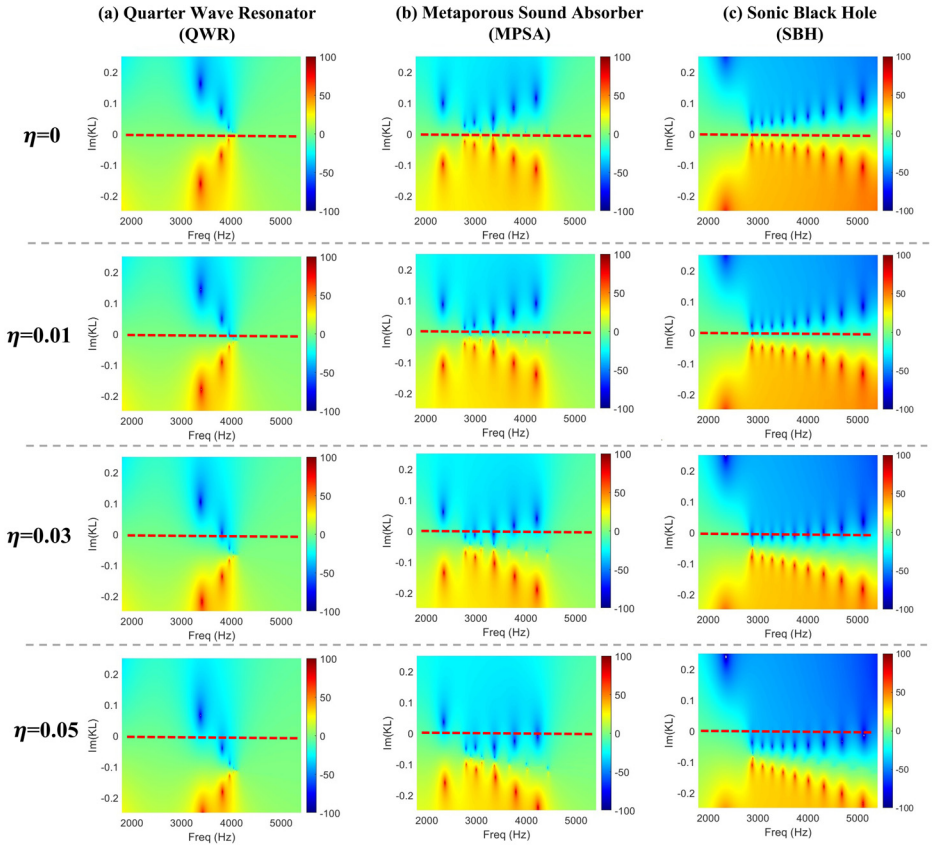

FIG. 7. (Color online) Complex frequency representation of sound reflection coefficient $20\log_{10}(|R|)$ for (a) QWR, (b) MPSA, and (c) SBH with varying levels of air damping: $\eta = 0$, 0.01, and 0.03–0.05.

analyzed here, it is worth noting that the narrow air channels between the partitions (i.e., ΔL=1.5 mm for $N = 20$) essentially provide visco-thermal loss effect. This explains why a previous SBH experiment can achieve high sound absorption coefficient without the inclusion of any additional porous material (see Ref. 23).

B. Effect of total length *L*

The effect of SBH total length L on its sound absorption is now analyzed with L varying from 0.015 to 0.06 m. The distance between two partitions, ΔL, that is also the length of the discretised layers, is kept at a constant value of 0.15 mm. Hence, the number of partitions in each case is $N = 10$ for $L = 0.015$ m, $N = 20$ for $L = 0.03$ m, and $N = 40$ for $L = 0.06$ m, respectively. Based on our prior understanding that SBH does not rely on large damping loss to establish substantial sound absorption, a moderate value of damping loss factor $\eta = 0.03$ is chosen in the comparisons. As shown in the first row of Fig. 11, the slow-sound pattern is more uniform with longer SBH, primarily due to a greater number of layers. The sound speed reduction in the longest SBH with the greatest number of layers is almost continuous and evenly distributed. Comparing the complex frequency planes of different cases in the second row shows that the resonance modes in the short SBH are more isolated, while those of the longest SBH almost coalesce into a continuous line. For frequencies above 3000 Hz, the sound absorption coefficient for the shortest SBH with $L = 0.015$ m is generally high, and the ups and downs can be identified from the resonances on the complex frequency plane. The third row shows that as L increases, the sound absorption coefficient improves significantly. For $L = 0.06$ m,

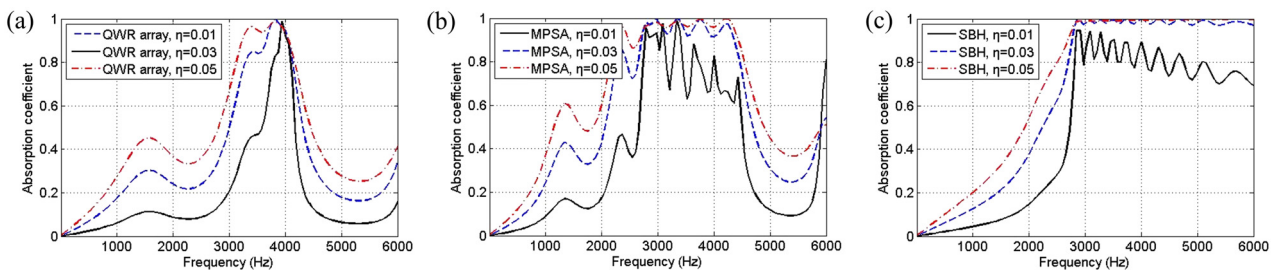

FIG. 8. (Color online) Effect of damping loss factor on the absorption coefficient of (a) QWR array, (b) MPSA, and (c) SBH. The air damping loss factor varies: $\eta = 0.01$, 0.03, and 0.05.

JASA
https://doi.org/10.1121/10.0021880

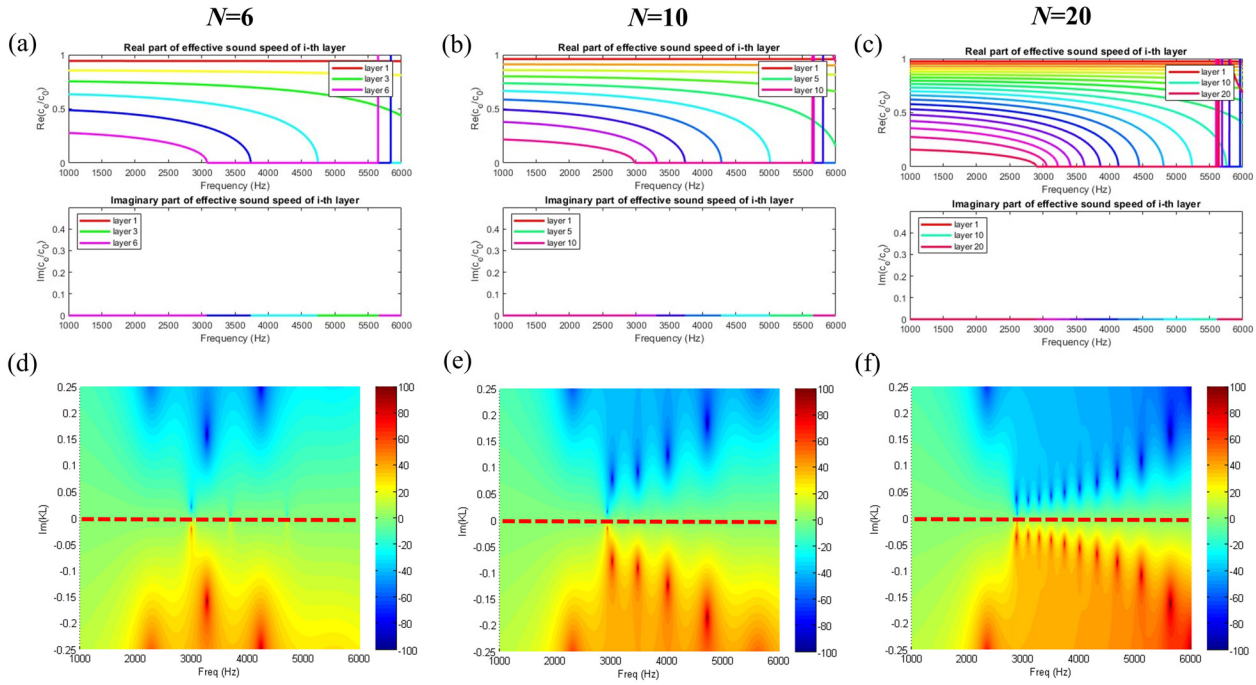

FIG. 9. (Color online) Effect of layer numbers N on the sound speed reduction and critical coupling condition. Linear SBH with $m = 1$; damping is not included with $\eta = 0$. (a)–(c) The effective sound speed of the ith layer, $N = 6$, 10, and 20, respectively. (d)–(f) Representation of $20\log10(|R|)$ in the complex frequency plane, $N = 6$, 10, and 20, respectively.

the absorption coefficient of SBH becomes a flat curve with $\alpha = 1$ without showing any fluctuations. The characteristic impedance plots confirm the role of impedance matching conditions in achieving the ideal sound absorption.

Figure 12 further compares the sound absorption coefficients for linear SBH with three different lengths. For frequencies above 3000 Hz, longer SBH with a greater number of layers performs better. For frequencies below 3000 Hz, longer SBH also shows significant improvement in terms of the low-frequency performance. To achieve an effective sound absorption of $\alpha > 0.5$, the shortest SBH starts from 2550 Hz, which shifts earlier to 2250 Hz and then to 1900 Hz by doubling the length L twice. These observations suggest that the cut-on frequency for SBH effect to take place is linked to its total length. Longer SBHs allow sound absorption to start at a lower frequency, which agrees with

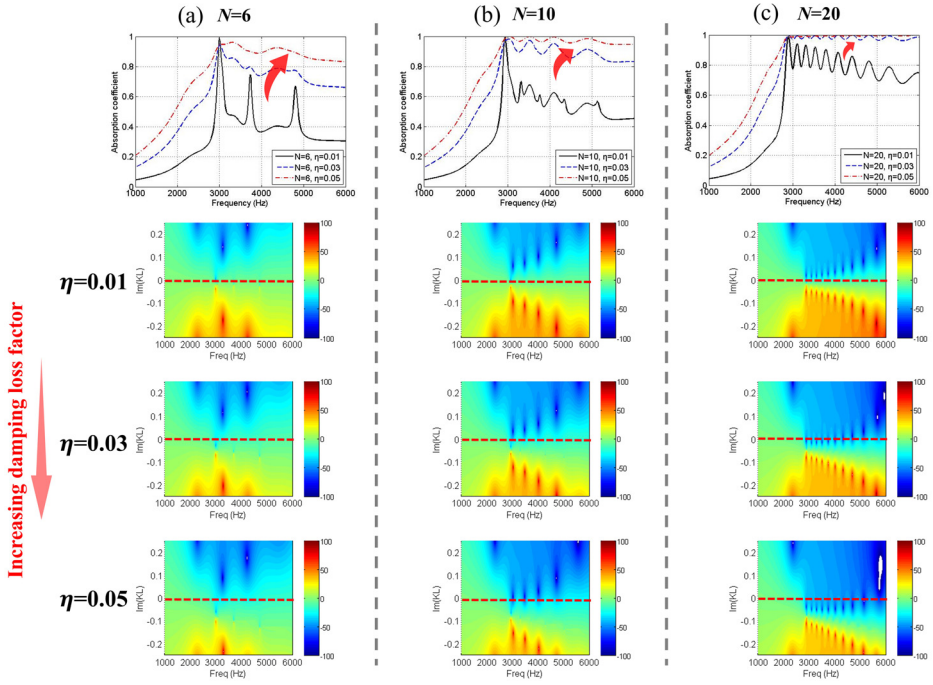

FIG. 10. (Color online) Effect of damping loss factor η on the SBH absorption with different layer numbers N. (a)–(c) Comparison of sound absorption coefficient and complex frequency plane representation for $N = 6$, 10, and 20, respectively.

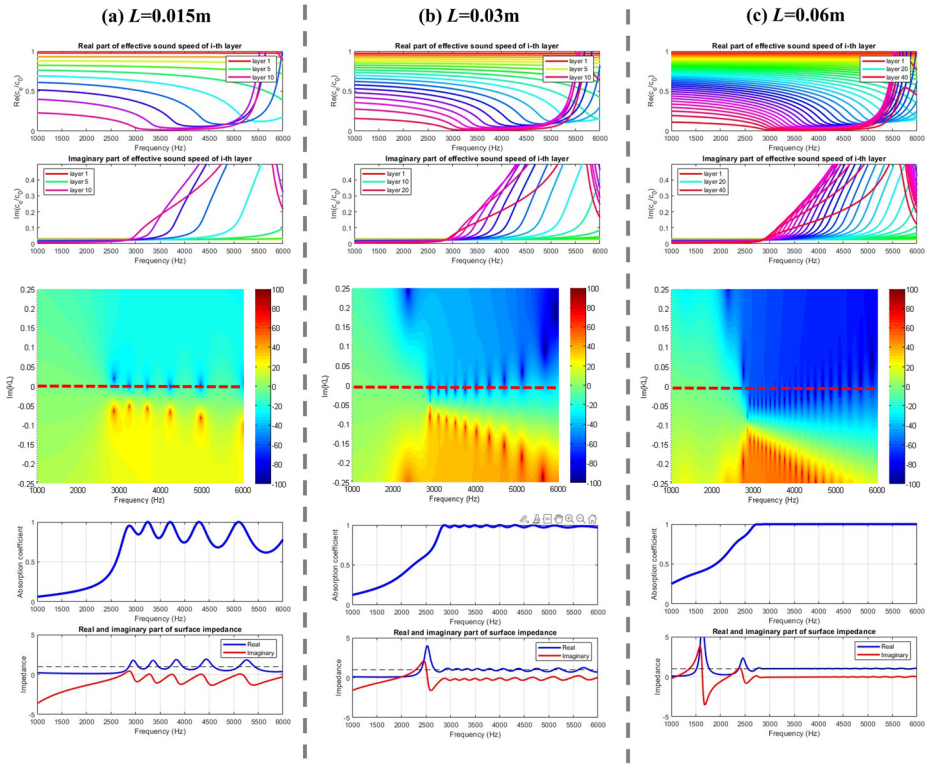

FIG. 11. (Color online) Effect of SBH total length L on the slow-sound pattern (first row), complex frequency plane results (second row), and absorption coefficient and impedance matching condition (third row): linear SBH case with $m=1$, η =0.03. The total length L and the corresponding layer numbers are (a) $L=0.015$ m, $N=10$; (b) $L=0.03$ m, $N=20$; and (c) $L=0.06$ m, $N=40$, respectively.

previous theoretical analyses.[18,23] However, as longer SBHs occupy larger space, a design trade-off may be necessary to achieve a balance between low-frequency performance and a realistic SBH size. Overall, these results demonstrate that increasing the length of the SBH leads to improved sound absorption properties, primarily due to the greater number of layers and more uniform slow-sound pattern. The findings have practical implications for designing SBHs with high absorption properties in various applications, such as noise control in buildings and transportation systems.

C. Effect of SBH profile order *m*

This section presents the analysis of the effect of SBH profile order m on the sound absorption coefficient. Three cases are considered here, with the SBH profile following linear, quadratic, and cubic variations represented by $m=1$, $m=2$, and $m=3$, respectively. The unit cell dimensions and the damping loss factor are fixed as $L=0.03$ m, $H=0.03$ m, and $\eta=0.03$, and the number of layers is set at $N=20$. The

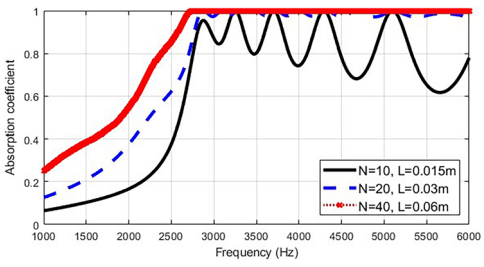

FIG. 12. (Color online) Comparison of sound absorption coefficients for linear SBH with varying total lengths: $L=0.015$ m, $L=0.03$ m, and $L=0.06$ m, respectively. The damping loss factor is taken as $\eta=0.03$.

varying trend of the inner height h_i of the ith discretised layer is shown in Fig. 13(a), where the radius decay from H to zero is more rapid with cubic variation $m=3$.

Figure 13(b) compares the sound absorption coefficient curves for the three cases, where the effective frequency region shifts to the left with increasing order m. For the linear case $m=1$, the main absorption range is from 3000 to 6000 Hz, with a flat curve nearing 1. For the quadratic $m=2$, the effective absorption with $\alpha > 0.8$ starts earlier from 2000 Hz. The last curve for the cubic case $m=3$ is further shifted to lower frequencies, while the higher-frequency end above 4000 Hz shows a slight drop. These results suggest that the profile of the SBH can be carefully tuned to balance the low- and high-frequency absorption performance.

Figures 14 and 15 further present the variation of sound speed and the complex frequency analyses to explain the observed trends, with Fig. 14 corresponding to the lossless case $\eta=0$ and Fig. 15 corresponding to the lossy case $\eta=0.03$. It can be seen that before damping is introduced, the slow-sound effect is concentrated more at the lower-frequency region with a higher-order profile. This is because the partitions in the higher-order SBH increase more rapidly; thus, h_i for the same layer is shorter, and sound propagation speed is compressed more heavily. The zero-pole pairs identified from the complex frequency plane also show that the resonances in higher-order SBH appear at lower frequencies. However, as profile order m increases, the distribution of resonances is not as uniform as the linear case. The zero-pole pairs are slightly away from the real frequency axis, implying that to achieve ideal absorption, more damping is required for SBHs with higher orders.

https://doi.org/10.1121/10.0021880

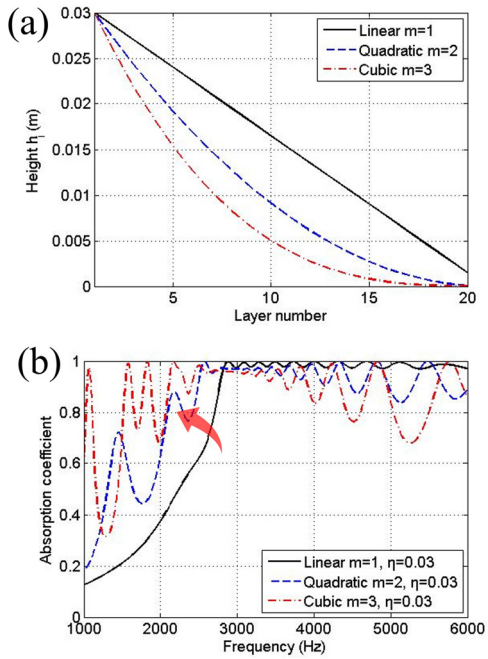

FIG. 13. (Color online) Comparison of sound absorption coefficients for SBH with linear, quadratic, and cubic profiles with $m=1$, $m=2$, and $m=3$, respectively.

Figure 15 displays the effect of damping loss factor $\eta=0.03$ on the sound speed reduction and complex frequency plane for the linear, quadratic, and cubic SBHs. The slow-sound patterns are consistent with those observed in Fig. 14, and damping lifts up the imaginary part of the effective speed to establish sound absorption. By comparing the second row of Fig. 15 against the sound absorption coefficient plots in Fig. 13(b), the direct relationship between sound absorption peaks and resonances on the complex frequency planes can be seen. For $m=1$, all the resonances above 3000 Hz are critically coupled and lie on the real frequency axis after damping is introduced. For $m=2$, adding damping enhances sound absorption between 2000 and 3000 Hz as evident by the movement of the zeros, and the resonances above 3000 Hz are evenly distributed. As a result, the absorption curve is flat and covers the widest frequency band. For $m=3$, the zeros are dragged closer to the zero axis with the addition of damping; however, they are mostly crowded between 2000 and 4000 Hz, and the distribution above 4000 Hz is sparse. As a result, the sound absorption coefficient shows distinct peaks rather than a flat curve. Although slight ups and downs are observed above 4000 Hz, the resonance modes remain critically coupled, as seen in Fig. 15(c); hence, the absorption coefficient remains above 0.8.

The comparison here shows the potential for tuning the effective frequency range by altering the geometric profile and damping loss factor of SBH. Furthermore, it is noteworthy that the geometric order m need not be integers; nor does the retarding profile need to be completely continuous. The design principles based on progressive slow-sound and critically coupled modes provide general guidelines for design optimization.

V. DISCUSSION

In summary, we have presented an investigation into the physical basis and principles of SBH by analyzing the changes in the sound propagation speed and the effective medium properties in the constituting layers using an effective medium approach, highlighting its unique features and several advantages. We have shown that the progressive slow-sound effect in SBH is achieved by the continuous increase in partition height and decrease in duct radius. This results in a more evenly distributed and closer-to-real-axis distribution of zero-poles in the complex frequency plane, requiring much less damping than other types of resonant sound absorbers. Note that the advantages of SBH over the compared cases of QWR and MPSA are concluded based on the geometries selected in this study. Further investigations may be required to determine whether these advantages hold true in other geometric settings. Additionally, the cut-on frequency and sound absorption performance of SBH can be easily tuned by adjusting the design variables, which represent some advantages for practical application.

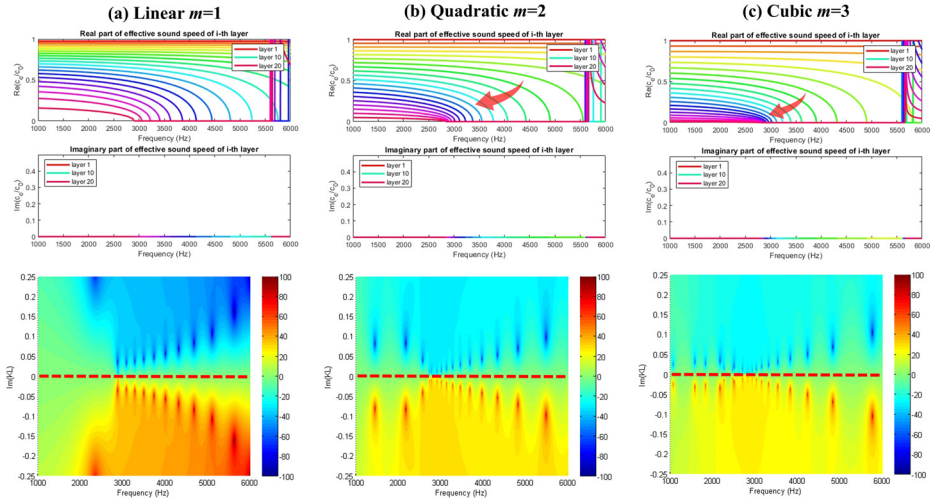

FIG. 14. (Color online) Effect of SBH order m on the sound speed reduction and critical coupling condition, lossless case with damping loss factor $\eta=0$. The sound speed of the ith layer and complex frequency plane representation for the linear case $m=1$, quadratic case $m=2$, and cubic case $m=3$ are displayed in (a), (b), and (c), respectively.

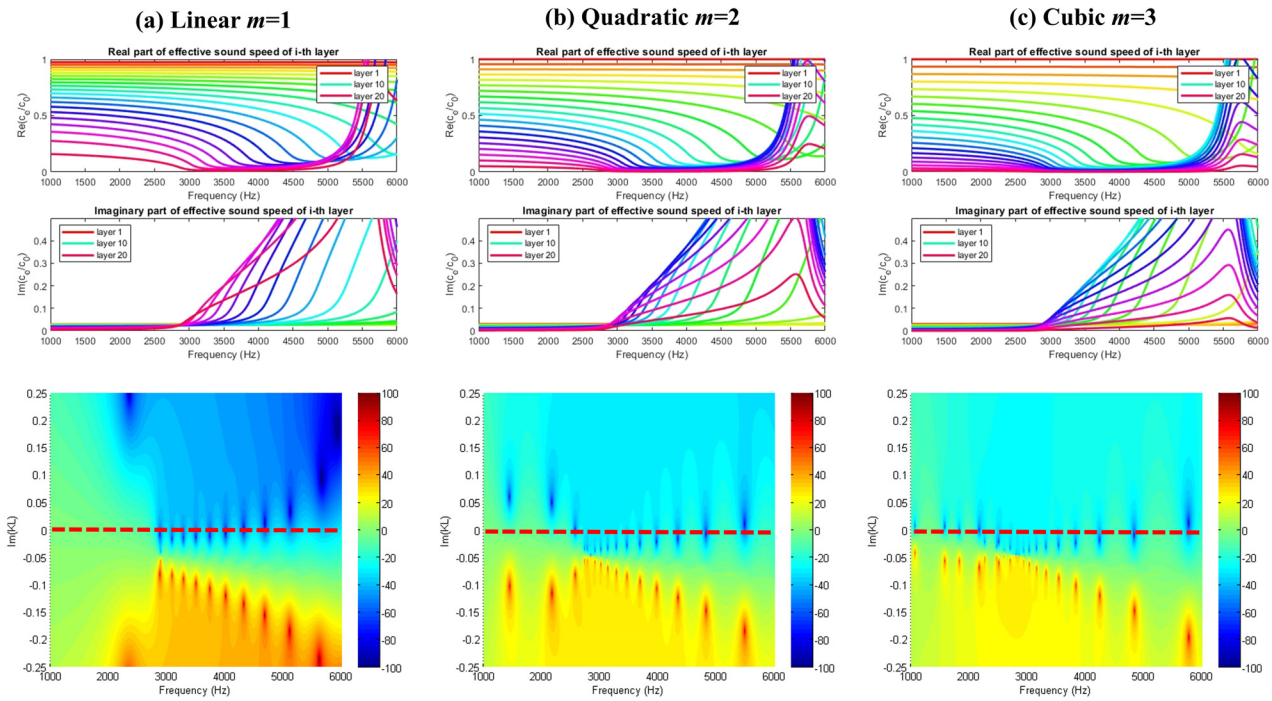

FIG. 15. (Color online) Effect of SBH order m on the sound speed reduction and critical coupling condition, lossy case with damping loss factor $\eta = 0.03$. The sound speed of the ith layer and complex frequency plane representation for the linear case $m = 1$, quadratic case $m = 2$, and cubic case $m = 3$ are displayed in (a), (b), and (c), respectively.

It is important to note that the design principles of SBH differ significantly from traditional metamaterial absorbers, such as metaporous absorbers, which rely on cascading multiple layers of resonators to achieve combined absorption in subdivided frequencies. The previous approach can lead to overlapped resonances and challenges in design optimization, resulting in the need for tedious design iterations and excessive damping to avoid destructive coupling in sound absorption.[11] In contrast, SBH design starts with selecting the retarding profile of the duct and number of layers to ensure smooth sound speed reduction and rainbow-like trapping. This leads to a more focused sound energy in the SBH structure and easier dissipation due to low radiation leakage. The critical coupling condition can then be effectively achieved by including porous materials or by the inherent damping between the narrow partitions. As the analyses imply, the broadband sound absorption potential of SBH is geometrically determined by the SBH profile and subsequently fulfilled or enhanced by additional damping. As a final remark, although this study does not include an experimental section, the authors have previously measured many SBH samples and achieved good accuracy between simulations and experiments. Interested readers can refer to Refs. 23 and 25 for sound absorption and transmission measurements of SBH samples using impedance tubes and Ref. 27 for the measurement of transient sound wave propagation in the time domain.

VI. CONCLUSIONS

This study presents a comprehensive investigation into the slow-sound effect and critical coupling condition in the SBH structure for sound absorption in air. Traditionally, the sound absorption mechanisms of foams or acoustic metamaterials are limited to flow resistance or resonance. The SBH achieves broadband total absorption with a unique geometric profile, where rainbow-like sound speed deceleration and uniform distribution of system resonances are realized across its constituting layers. Numerical models based on the effective medium approach were developed. The broadband sound absorption performance, the effect of system parameters, and the dependence on geometry and damping were fully elucidated through comparisons with traditional resonant sound absorbers composed of quarter-wave resonators and metaporous unit cells.

From the parametric analyses, the study identifies that the length and order of the SBH profile are two critical parameters that affect the absorption performance of the SBH structure. The length of the SBH structure is found to affect the cut-on frequency. Longer SBH structures with smoothly varying heights allow for a more even distribution of the slow-sound effect, which results in a lower cut-on frequency for high absorption. Different orders of the SBH profile lead to different frequency responses, with higher-order profiles showing a more intense slow-sound effect at lower frequencies and lower-order profiles being more effective at higher frequencies. This suggests that the profile of SBH can be carefully tuned to strike a balance between low- and high-frequency absorption performance.

Overall, this study provides a detailed explanation of the working mechanisms of SBH for sound absorption in air, revealing new physical insights and defining critical conditions to achieve a successful design. It emphasizes the

https://doi.org/10.1121/10.0021880

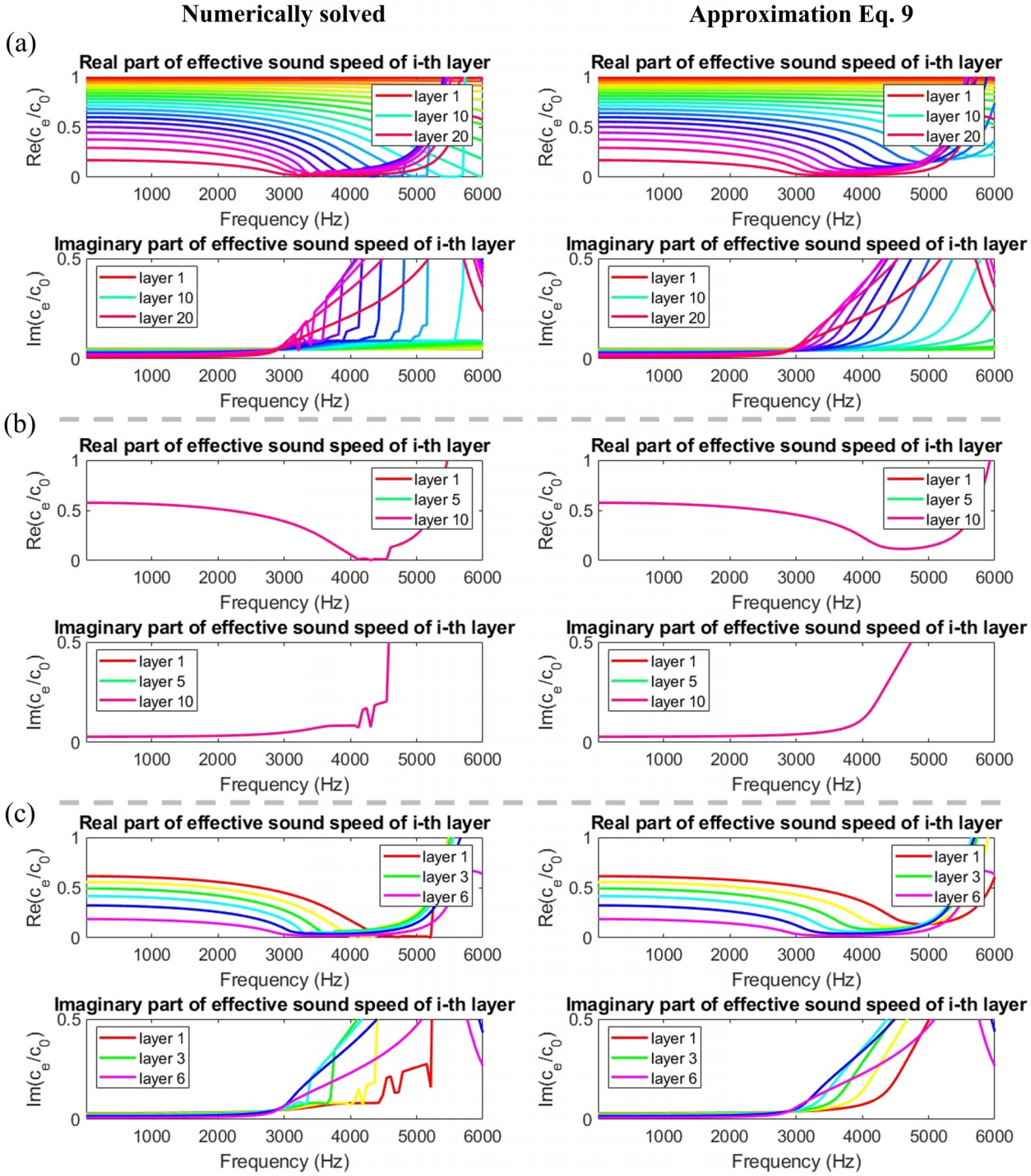

FIG. 16. (Color online) Comparison of the sound propagation speed (both the real and imaginary parts) of the *i*th layer solved numerically or obtained by approximations using Eq. (9). (a) SBH; (b) QWR array; (c) MPSA.

necessity of progressive slow-sound and even distribution of resonances by the discretised layers to achieve critical coupling conditions with less damping. SBH structures show many potential advantages over traditional sound-absorbing materials and even acoustic metamaterials. This study discovers the essential physics relevant to the SBH, potentially broadening its utility in various fields and paving the way for the development of more efficient sound-absorbing materials for practical applications.

ACKNOWLEDGMENTS

This research is supported by the Research Grants Council of Hong Kong under Grant No. PolyU 15201822. Y.X. acknowledges start-up funding support from the Department of Mechanical Engineering and the Hong Kong Polytechnic University. The authors declare that they have no known competing financial interests or personal relationships that could have appeared to influence the work reported in this paper.

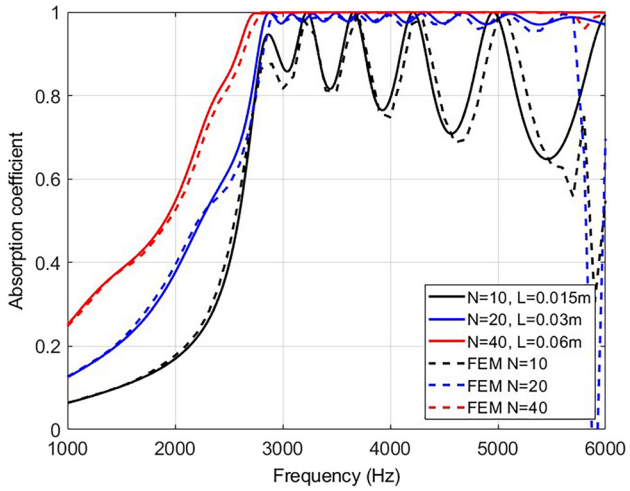

FIG. 17. (Color online) Validation of the theoretical model by comparing the sound absorption coefficients calculated using the effective medium approach to the FEM results, for the cases of SBH with different total lengths.

APPENDIX

The comparison between the effective sound speeds in the discretised layers, obtained based on approximations given in Eq. (9), and those obtained through numerical solutions is presented in Fig. 16. It can be seen that the trend of the real part is in good agreement, particularly for frequencies up to approximately 4000 Hz. This is consistent with the small angle assumption made by letting $\tan(k_{i,A,y}h_i) \approx k_{i,A,y}h_i$. At very high frequencies, the numerical solutions exhibit some irregularities, which may be attributed to the selection of the root searching strategy employed by the solver.

As a means of validating the theoretical model presented in Sec. II, the calculated sound absorption coefficients obtained through the effective medium approach [using Eqs. (11)–(13)] are compared to results obtained through finite element method (FEM) simulations in Fig. 17. The results in Fig. 12 were used, taking into account the effect of linear SBH with different total lengths. The FEM calculations were carried out using COMSOL Multiphysics, which has been extensively validated in previous studies against analytical solutions or experiments, thereby ensuring accuracy. The results demonstrate excellent agreement for all compared cases, thus, confirming the validity of the theoretical analysis. It should be noted that the FEM curves exhibit a sudden drop starting from 5600 Hz, which can be attributed to the duct cut-off frequency at $c_0/2/0.03 = 5600$ Hz. Interested readers can refer to Refs. 23, 25, and 27 for experimental measurement of SBH performances in previous studies.

[1]J. Allard and N. Atalla, *Propagation of Sound in Porous Media: Modelling Sound Absorbing Materials*, 2nd ed. (Wiley, New York, 2009).
[2]X. Yu, Z. Lu, and W. Zhai, "Enhancing the flow resistance and sound absorption of open-cell metallic foams by creating partially-open windows," Acta Mater. **206**, 116666 (2021).
[3]J. W. Chua, X. Li, T. Li, B. W. Chua, X. Yu, and W. Zhai, "Customisable sound absorption properties of functionally graded metallic foams," J. Mater. Sci. Technol. **108**, 196–207 (2022).
[4]D.-Y. Maa, "Microperforated-panel wideband absorbers," Noise Control Eng. J. **29**, 77–84 (1987).
[5]D.-Y. Maa, "Potential of microperforated panel absorber," J. Acoust. Soc. Am. **104**, 2861–2866 (1998).
[6]X. Li, X. Yu, J. W. Chua, and W. Zhai, "Harnessing cavity dissipation for enhanced sound absorption in Helmholtz resonance metamaterials," Mater. Horiz. **10**, 2892–2903 (2023).
[7]X. Li, X. Yu, and W. Zhai, "Additively manufactured deformation-recoverable and broadband sound-absorbing microlattice inspired by the concept of traditional perforated panels," Adv. Mater. **33**, 2104552 (2021).
[8]N. Fang, D. Xi, J. Xu, M. Ambati, W. Srituravanich, C. Sun, and X. Zhang, "Ultrasonic metamaterials with negative modulus," Nat. Mater. **5**, 452–456 (2006).
[9]V. M. García-Chocano, R. Graciá-Salgado, D. Torrent, F. Cervera, and J. Sánchez-Dehesa, "Quasi-two-dimensional acoustic metamaterial with negative bulk modulus," Phys. Rev. B **85**, 184102 (2012).
[10]J. Yang, J. S. Lee, and Y. Y. Kim, "Metaporous layer to overcome the thickness constraint for broadband sound absorption," J. Appl. Phys. **117**, 174903 (2015).
[11]J. Yang, J. S. Lee, and Y. Y. Kim, "Multiple slow waves in metaporous layers for broadband sound absorption," J. Phys. D: Appl. Phys. **50**, 015301 (2017).
[12]N. Gao, J. Wu, K. Lu, and H. Zhong, "Hybrid composite meta-porous structure for improving and broadening sound absorption," Mech. Syst. Signal Process. **154**, 107504 (2021).
[13]G. Ma, M. Yang, S. Xiao, Z. Yang, and P. Sheng, "Acoustic metasurface with hybrid resonances," Nat. Mater. **13**, 873–878 (2014).
[14]V. Romero-García, G. Theocharis, O. Richoux, and V. Pagneux, "Use of complex frequency plane to design broadband and sub-wavelength absorbers," J. Acoust. Soc. Am. **139**, 3395–3403 (2016).
[15]N. Jiménez, V. Romero-García, V. Pagneux, and J.-P. Groby, "Rainbow-trapping absorbers: Broadband, perfect and asymmetric sound absorption by subwavelength panels for transmission problems," Sci. Rep. **7**, 13595 (2017).
[16]H. Long, C. Liu, C. Shao, Y. Cheng, K. Chen, X. Qiu, and X. Liu, "Subwavelength broadband sound absorber based on a composite meta-surface," Sci. Rep. **10**, 13823 (2020).
[17]X. Yu, Y. Tong, J. Pan, and L. Cheng, "Sub-chamber optimization for silencer design," J. Sound Vib. **351**, 57–67 (2015).
[18]M. A. Mironov and V. V. Pislyakov, "One-dimensional acoustic waves in retarding structures with propagation velocity tending to zero," Acoust. Phys. **48**, 347–352 (2002).
[19]M. Mironov and V. Pislyakov, "One-dimensional sonic black holes: Exact analytical solution and experiments," J. Sound Vib. **473**, 115223 (2020).
[20]A. Pelat, F. Gautier, S. C. Conlon, and F. Semperlotti, "The acoustic black hole: A review of theory and applications," J. Sound Vib. **476**, 115316 (2020).
[21]B. M. P. Chong, L. B. Tan, K. M. Lim, and H. P. Lee, "A review on acoustic black-holes (ABH) and the experimental and numerical study of ABH-featured 3D printed beams," Int. J. Appl. Mech. **09**, 1750078 (2017).
[22]O. Guasch, M. Arnela, and P. Sánchez-Martín, "Transfer matrices to characterize linear and quadratic acoustic black holes in duct terminations," J. Sound Vib. **395**, 65–79 (2017).
[23]Y. Mi, W. Zhai, L. Cheng, C. Xi, and X. Yu, "Wave trapping by acoustic black hole: Simultaneous reduction of sound reflection and transmission," Appl. Phys. Lett. **118**, 114101 (2021).
[24]T. Bravo and C. Maury, "Broadband sound attenuation and absorption by duct silencers based on the acoustic black hole effect: Simulations and experiments," J. Sound Vib. **561**, 117825 (2023).
[25]X. Zhang and L. Cheng, "Broadband and low frequency sound absorption by Sonic black holes with Micro-perforated boundaries," J. Sound Vib. **512**, 116401 (2021).
[26]X. Liang, H. Liang, J. Chu, W. Wang, N. Li, Z. Yang, G. Zhou, N. Gao, C. Hu, and Z. Zhou, "A modified sonic black hole structure for improving and broadening sound absorption," Appl. Acoust. **210**, 109440 (2023).
[27]S. Li, J. Xia, X. Yu, X. Zhang, and L. Cheng, "A sonic black hole structure with perforated boundary for slow wave generation," J. Sound Vib. **559**, 117781 (2023).
[28]J.-P. Groby, W. Huang, A. Lardeau, and Y. Aurégan, "The use of slow waves to design simple sound absorbing materials," J. Appl. Phys. **117**, 124903 (2015).

[29]Z. Li, W. Zhai, X. Li, X. Yu, Z. Guo, and Z. Wang, "Additively manufactured dual-functional metamaterials with customisable mechanical and sound-absorbing properties," Virtual Phys. Prototyp. **17**, 864–880 (2022).
[30]M. Malléjac, P. Sheng, V. Tournat, V. Romero-García, and J.-P. Groby, "Slow-sound-based delay-line acoustic metamaterial," Phys. Rev. Appl. **17**, 044035 (2022).
[31]N. Jiménez, V. Romero-García, V. Pagneux, and J.-P. Groby, "Quasiperfect absorption by subwavelength acoustic panels in transmission using accumulation of resonances due to slow sound," Phys. Rev. B **95**, 014205 (2017).
[32]N. Jiménez, W. Huang, V. Romero-García, V. Pagneux, and J.-P. Groby, "Ultra-thin metamaterial for perfect and quasi-omnidirectional sound absorption," Appl. Phys. Lett. **109**, 121902 (2016).